2D myocardial deformation imaging based on RF-based non-rigid image registration

Bidisha Chakraborty*, Zhi Liu†, Brecht Heyde*, Jianwen Luo† and Jan D'hooge*
*Cardiovascular Imaging and Dynamics, KU Leuven, Leuven, Belgium
†Department of Biomedical Engineering, Tsinghua University, Beijing
Email: bidisha.chakraborty@kuleuven.be

***Abstract*—Myocardial deformation imaging is a well-established echocardiographic technique for the assessment of myocardial function. Although some solutions make use of speckle tracking of the reconstructed B-mode images, others apply block matching on the underlying radio-frequency (RF) data in order to increase sensitivity to small inter-frame motion and deformation. However, for both approaches, lateral motion estimation remains a challenge due to the relatively poor lateral resolution of the ultrasound image in combination with the lack of phase information in this direction. Hereto, non-rigid image registration (NRIR) of B-mode images has previously been proposed as an attractive solution. However, hereby, the advantages of RF-based tracking were lost. The aim of this study was therefore to develop an NRIR motion estimator adopted to RF data sets. The accuracy of this estimator was quantified using synthetic data and was contrasted against a state of the art block matching solution. The results show that RF-based NRIR outperforms BM in terms of tracking accuracy particularly, as hypothesized, in the lateral direction. Finally, this RF-based NRIR algorithm was applied clinically, illustrating its ability to estimate both in-plane velocity components *in-vivo*.**

***Index Terms*—RF image, non-rigid registration, strain, cardiac, block matching**

I. Introduction

Myocardial deformation imaging has become an established echocardiographic technique for the assessment of global and regional myocardial function [1] and has shown its clinical value in a variety of clinical settings, e.g., in the detection of patients with acute heart failure [2], myocardial ischemia [3], quantification of dyssynchrony and prediction of response to CRT [4], [5].

From a technical perspective, different approaches towards ultrasound deformation imaging have been proposed which can be classified into three major categories: speckle tracking, phase sensitive methods and non-rigid image registration (NRIR). Speckle tracking assumes that speckle patterns are preserved between subsequent images and can therefore be used as acoustic markers to track the motion of the underlying tissue. Two popular speckle tracking approaches are block matching (BM) [6] and optical flow [7], [8]. In phase sensitive methods, motion is rather retrieved from the change in local phase between image pairs [9]. It can be considered as a generalization to multiple dimensions of the typical Doppler-based motion estimator [10]. Finally, NRIR is a popular method in the image processing community, where motion is estimated iteratively by minimizing a cost function that imposes boundary conditions on the motion field *during* the motion estimation process while this is typically done a posteriori for the other approaches.

In principle, any of these motion estimation methods can be applied to either the high frequency raw radio-frequency (RF) images, their corresponding low frequency envelope images (amplitude demodulated RF signals) or the scan-converted B-mode images (after interpolation and subsampling). While all of the above mentioned methods have been applied on the reconstructed B-mode images (e.g., block matching [4], [11]–[13], phase sensitive [14] and NRIR [15]), the main advantage of the latter approach seems to be a more robust estimation of the lateral motion component [16]. Indeed, lateral motion estimation is particularly challenging given the relatively poor lateral image resolution in combination with the lack of phase information in this direction in a conventional ultrasound recording and therefore benefits particularly from imposing boundary conditions on the motion field during the estimation process.

It is well known that motion estimation on the underlying RF data results in more accurate estimates for small inter-frame motions [17], [18]. In addition, it has been shown that the estimated elastographic signal-to-noise ratio (eSNR) of cardiac strain estimated on the RF signals are higher than the ones estimated from the corresponding envelope signals [19]. Theoretically, these improved estimates in RF images can only be attributed to the phase information available in the axial direction compared to its corresponding envelope signal. Since, a 2D motion estimator typically couples the axial and lateral estimates; a precise axial estimate likely positively impacts the accuracy of the lateral estimate. As such, it is not surprising to see that both block matching [20]–[24] and phase sensitive [25] approaches have been applied on RF data as well. However, despite the promising findings of NRIR in terms of lateral motion estimation, to date, NRIR has only been applied on intravascular (IV) RF data [26]. Nevertheless, the vascular tissue experiences a relatively smaller (0.1%-10%) and simpler deformation, in contrast to cardiac tissue and therefore the theoretical advantages of processing RF data for cardiac deformation imaging still needs to be explored.

Therefore, the main goal of this work was to develop an RF-based NRIR motion estimator for cardiac applications, which brings along specific challenges. Firstly, a typical B-mode image is much smaller (e.g., 512× 512 pixels) compared to a typical RF frame (e.g., 8,000 samples × 200 lines),

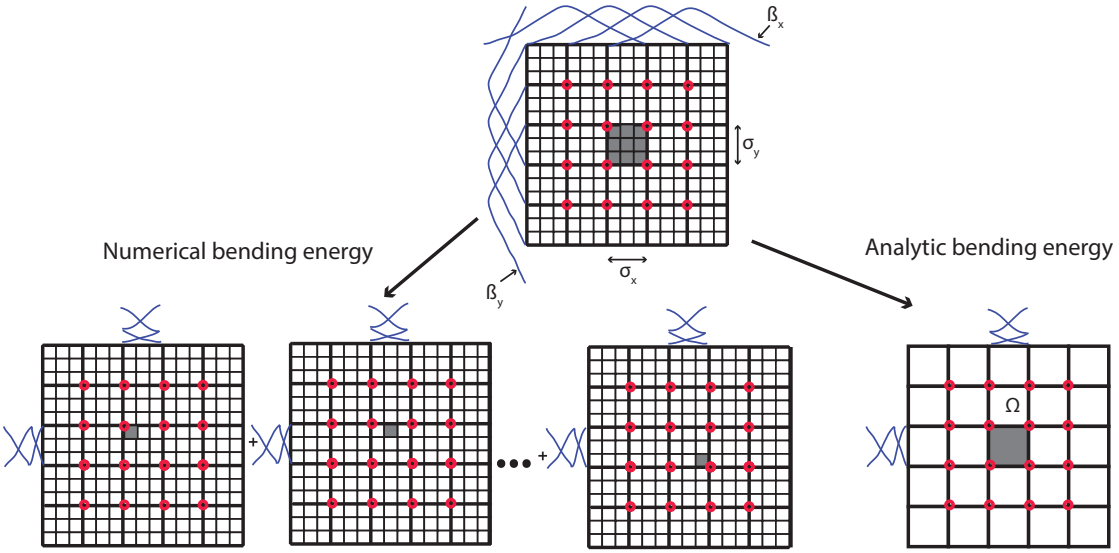

Fig. 1. Schematic overview of the computation of the bending energy (BE) in an example shaded region (Ω) consisting of nine pixels and the four associated third-order B-splines in each direction (blue) supported by the sixteen control grid points (red). The BE contribution of this shaded Ω is a function of the B-spline pieces and the inter-grid spacing σ. To numerically compute (left) this BE, the BE for all nine pixels has to be computed individually and summed. On the other hand, for the analytic computation (right), the BE value of Ω (shaded) can be precomputed once and stored in form of three matrices, making the calculation of BE computationally efficient.

which leads to a significant increase in computational burden. Hereto, an analytic expression for the regularization term in the cost function of the registration framework is proposed to replace its numeric analogue. Secondly, in contrast to the pixels being isotropic for B-mode images, RF pixels are very anisotropic with direct consequences for the optimal mathematical representation of the motion field in the registration framework. Using synthetic data sets mimicking physiologic cardiac motion and deformation conditions, the accuracy of the proposed solution is demonstrated. In addition, the same synthetic data are used to contrast the proposed RF-based NRIR with a state of the art RF-based block matching algorithm. Finally, the proposed RF-based NRIR algorithm was applied clinically, illustrating its ability to estimate both in-plane velocity components *in-vivo*. Preliminary results on pilot studies of applying NRIR to RF data were previously reported by our group in [27] and [28]. However, these studies used limited motion modes and did not systematically test the impact of the inter-frame motion/deformation magnitude on the accuracy of the resulting motion/deformation estimates. Moreover, our previous reports did not go through a rigorous optimization process of the optimal NRIR settings. In addition, in previous reports, no comparison against block matching was performed and finally, the proposed approach was not previously tested *in-vivo*. All of these are novel contributions of the current manuscript.

II. Method

A. NRIR

During non-rigid image registration, a moving image $\mathrm{I_M}$ is deformed to spatially align with a fixed image $\mathrm{I_F}$. The inter-frame myocardial displacement field $\mathbf{T}_\xi = (\mathrm{T_x}, \mathrm{T_y})$ is computed at every pixel $\mathbf{r} = [\mathrm{x}, \mathrm{y}]$ and is modeled as a tensor product of 2D cubic B-splines β^3_ξ ($\xi \in (\mathrm{x}, \mathrm{y})$) [29]:

$$\mathbf{T}_\xi(\mathbf{r}) = \sum_{\mathrm{i}\in \mathrm{N_i}} \sum_{\mathrm{j}\in \mathrm{N_j}} \boldsymbol{\mu}_{\mathrm{ij}} \beta^3_{\mathrm{x}} \left(\frac{\mathrm{x} - \kappa^{\mathrm{ij}}_{\mathrm{x}}}{\sigma_{\mathrm{x}}} \right) \beta^3_{\mathrm{y}} \left(\frac{\mathrm{y} - \kappa^{\mathrm{ij}}_{\mathrm{y}}}{\sigma_{\mathrm{y}}} \right) \quad (1)$$

where N_ξ denotes a set of control grid points within the compact support of the B-splines (β^3_ξ) and having an inter-grid spacing of σ_ξ.

$\mathbf{T}_\xi(\mathbf{r})$ is parametrized by B-spline coefficients $\boldsymbol{\mu}_{\mathrm{ij}}$, associated to every control point node. This set of coefficients is updated to optimum values, during an iterative optimization process by minimizing a cost function. In order to ensure a convergence to a global minimum in the optimization space, the images are registered in a multi-resolution framework [29], [30]. More specifically, a coarse-to-fine strategy is adopted where firstly, the transformation complexity is gradually increased in a transformation pyramid by decreasing the inter-grid spacings, σ_ξ between control points in subsequent levels. Secondly, in order to initially align the coarsest global structures and slowly introduce more detailed image features, the data complexity is gradually increased by building an image pyramid. This is done by convolving the image with a Gaussian scale space, where the size of the smoothing kernel is reduced at each scale of the image pyramid, and by simultaneously registering the RF image at the finest (topmost) and envelope images at the coarsest (bottommost) levels of the pyramid.

To efficiently optimize this large number of coefficients $\boldsymbol{\mu}_{\mathrm{ij}}$, a limited memory Broyden-Fletcher-Goldfarb-Shanno (LBFGSB) optimization routine with simple bounds is used. This optimizer is generally used for optimization of a large set of parameters [31].

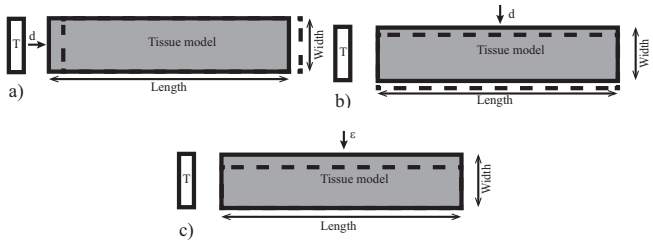

Fig. 2. Schematic illustration of the three different motion modes in the simulated tissue model in the Cartesian space: a) axial and b) lateral bulk motion with bulk displacement d and c) lateral compression with strain ε.

A general expression of the cost function used for optimization can be given as:

$$C = \mathrm{S} + \omega \mathrm{R} \tag{2}$$

where S is a similarity measure and R is a regularization term, weighted by a factor ω to adjust the strength of R. In our framework, the sum of squared differences (SSD) is used as a similarity measure S. SSD has been the choice of the similarity measure because of its good performance in monomodal registration and simplicity of its computation. Additionally, in order to penalize high curvature solutions of the displacement field ($\mathbf{T}_\xi$), a squared second order derivative of R associated with $\mathbf{T}_\xi$ is chosen as the bending energy (BE) penalty term [29].

The conventional numeric representation of (R) is denoted here by $\mathrm{R_N}$. This can be obtained by computation of the second order derivatives of the underlying transformation field at every pixel location, $\mathbf{r}$ in the image comprising of P pixels [29]:

$$\mathrm{R_N} = \frac{1}{\mathrm{P}} \sum_{\mathbf{r}} \sum_{\xi \in (\mathrm{x,y})} \left(\frac{\partial^2 \mathrm{T}_\xi}{\partial \mathrm{x}^2} \right)^2 + \left(\frac{\partial^2 \mathrm{T}_\xi}{\partial \mathrm{y}^2} \right)^2 + 2 \left(\frac{\partial^2 \mathrm{T}_\xi}{\partial \mathrm{x} \partial \mathrm{y}} \right)^2 \tag{3}$$

where the second order derivatives are obtained by a numeric central differencing scheme. It can be noted from the above expression that the overall computational complexity of $\mathrm{R_N}$ is proportional to the total number of pixels (P) present in the image and these computations are performed on the fly for each iteration of the optimizer.

B. Fast NRIR for application on RF data

An RF image has typically a much larger number of pixels than a typical B-mode image, making the evaluation of $\mathrm{R_N}$ computationally more demanding. As an alternative, the computation of R can be sped up by using a closed analytic solution, $\mathrm{R_A}$. In our previous work [32], we have demonstrated the application of $\mathrm{R_A}$ in *in-silico* cardiac data. This regularizer is inspired by previous developments proposed in [33]. Here, the computation of $\mathrm{R_A}$ is directly proportional to the number of regions Ω, that sum up to represent the whole transformation field as follows:

$$\mathrm{R_A} = \frac{1}{\mathrm{P}} \sum_{\Omega} \mathrm{R}_\Omega \tag{4}$$

where $\mathrm{R_A}$ is sum of individual contributions of the bending energy for each region R_Ω, which can be represented as:

$$\mathrm{R}_\Omega = \sum_{(\delta_\mathrm{x}, \delta_\mathrm{y})} \left(\boldsymbol{\mu}_\mathrm{i}{}^\mathrm{T} \mathrm{V}^{(\delta_\mathrm{x}, \delta_\mathrm{y})} \boldsymbol{\mu}_\mathrm{i} + \boldsymbol{\mu}_\mathrm{j}{}^\mathrm{T} \mathrm{V}^{(\delta_\mathrm{x}, \delta_\mathrm{y})} \boldsymbol{\mu}_\mathrm{j} \right) \quad \text{for} \quad (\delta_x + \delta_y = 2) \tag{5}$$

where $\boldsymbol{\mu}_\mathrm{i}$ and $\boldsymbol{\mu}_\mathrm{j}$ are vectors containing all the B-spline coefficients associated to the relevant control points for Ω in x and y directions respectively. Additionally, $\mathrm{V}^{(\delta_\mathrm{x}, \delta_\mathrm{y})}$ represent the matrices which can be precomputed on the basis of the inter-grid spacings σ_ξ. Since the contribution of the derivative of the BE penalty at every control point $\boldsymbol{\mu}_\mathrm{ij}$ depends on the physical spacings σ_ξ and these spacings remain constant at one particular pyramid level, the contribution of the BE of the whole Ω can be precomputed and stored in memory; only to be reused for computing the BE of the whole image. In case of 2D images, three of these matrices were precomputed and stored in memory for each grid resolution. For further details the reader is referred to [32].

The difference in computational burden between $\mathrm{R_N}$ and $\mathrm{R_A}$ is illustrated by an example in Fig. 1. At the top, the contribution of the BE between the control grid points (red) within the compact support of B-splines (blue) is shown by the shaded region, Ω (gray). For computation of $\mathrm{R_N}$ (bottom left) within Ω, Eq. (3) has to be evaluated at every pixel located within Ω, i.e., nine times in this example. In contrast, for computation of $\mathrm{R_A}$ (bottom right) within Ω, the matrices ($\mathrm{V}^{(\delta_\mathrm{x}, \delta_\mathrm{y})}$) in Eq. (5) need to be precomputed and stored only once and therefore can be reused to compute the contribution of the other non-shaded grid regions of the image.

III. RF-based NRIR experiments

A. In-silico data generation

To optimize and test the accuracy of the proposed RF-based NRIR motion estimator, synthetic data sets mimicking physiologic inter-frame motion/deformation magnitudes were generated. Hereto, a simple geometric model of the left ventricular septum in an apical echocardiographic view was constructed as a 2D, rectangular, homogeneous region of 100 mm $\times$ 20 mm in the axial and lateral directions respectively. This septal model was filled with 3 million scattering sites at random positions having a random scattering cross section in order to fulfill the requirements for fully developed speckle (i.e., at least 10 scattering sites per resolution cell) [34]. RF images sampled at 50 MHz were simulated using COLE [35], assuming a sector scan with an opening angle of 70° and using a phased array transducer with a center frequency of 3.4 MHz which resulted in RF images of 7,793 samples $\times$ 190 lines.

Three different motion modes were generated as schematically illustrated in Fig. 2: i) axial bulk motion (panel a), ii) lateral bulk motion (panel b) and iii) lateral deformation (panel c). The imposed inter-frame motion for the respective modes was chosen based on typical physiologic motions encountered in the heart, i.e., 15-150 mm/s [36]. Assuming a frame rate of 100 Hz, this results in an inter-frame displacement ranging from 0.15 mm to 1.5 mm; out of which 10 equidistant

values were tested. Similarly, inter-frame deformation was realistically estimated to be in the range of 1.17% to 1.97%; out of which 10 equidistant values were tested. Hereto, the systolic duration was estimated to last for about 300 ms for a normal heart beating at 80 bpm [37] during which the muscle thickens in the lateral direction within the range of 35% to 59% [38].

To account for the stochastic nature of the RF data, 10 independent speckle realizations were simulated for each of the displacement and deformation set-ups.

B. Accuracy of the RF-based NRIR

To quantitatively assess the performance of this algorithm, a region of interest (ROI) was chosen by excluding 5% of the model at the borders in order to avoid border effects. N points with a size of 300 × 200 (axial × lateral) were distributed within this ROI and deformation estimates at these points were interpolated from the transformation field containing motion estimates at each pixel of the RF image. Subsequently, the norm percentage error, $\Delta \mathrm{d}_i$ for each point i was calculated for both the axial and the lateral bulk motion modes as:

$$\Delta \mathrm{d}_i = \frac{||\mathbf{K}_{\mathrm{M}}^i - \hat{\mathbf{K}}_{\mathrm{M}}^i||_2}{||\mathbf{K}_{\mathrm{F}}^i - \mathbf{K}_{\mathrm{M}}^i||_2} \qquad \text{for } i \in 1 \ldots \mathrm{N} \tag{6}$$

with $\mathbf{K}_i$ and $\hat{\mathbf{K}}_i$ being the ideal and the estimated positions in Cartesian space respectively and the suffix F and M representing the locations of the points in the fixed and moving frames respectively. The mean and standard deviation of $\Delta \mathrm{d}_i$ were computed over the entire model and for all the modes with bulk displacements.

In case of lateral deformation, the estimated strain ($\hat{\varepsilon_j}$) at a given depth j was computed from these N points as:

$$\hat{\varepsilon_j} = \frac{\hat{\mathrm{L}}_{\mathrm{M}}^j - {\mathrm{L}_{\mathrm{F}}}^j}{{\mathrm{L}_{\mathrm{F}}}^j} \tag{7}$$

with ${\mathrm{L}_{\mathrm{F}}}^j$ and $\hat{\mathrm{L}}_{\mathrm{M}}^j$ being the distances between the outermost points in the lateral direction at a given depth j in the initial (i.e., I_{F}) and deformed (i.e., $\hat{\mathrm{I}}_{\mathrm{M}}$) images respectively. Subsequently, the relative strain errors at given depth were computed:

$$\Delta_{\varepsilon_j} = \frac{\hat{\varepsilon_j} - \varepsilon_j}{\varepsilon_j} \tag{8}$$

where ε_j is the applied reference strain.

Again, mean and standard deviation of the estimated Δ_{ε_j} were computed over the entire model and for all the modes with lateral deformation.

C. Parameter optimization

In order to optimize the parameter settings for the RF-based NRIR, two experiments were conducted using 6 of the synthetic data sets (i.e., 2 per motion mode at the extremities of the tested motion/deformation ranges):

Registration grid anisotropy: As pixels in the RF domain are anisotropic, an isotropic registration grid - as typically used for B-mode image registration [39] might sub optimally represent the true motion field. Indeed, the bending energy used as a regularizer would physically impose an anisotropic smoothness in the axial and lateral direction for an isotropic B-spline grid in the RF domain. In order to address this problem, several grid aspect ratios were tested ranging from 1:1 (axial:lateral) to 4:1 either by increasing σ_{x} (case A) or by reducing σ_{y} (case B).

Bending energy weight: Obviously, an important parameter in the registration framework is ω which defines the balance between the image information and the prior boundary conditions. Hereto, different settings for ω were tested, i.e., 1×10^6, 5×10^6 and 5×10^8. This range was chosen based on a rough initial visual inspection of the tracking results. In addition, a hybrid setting was tested in which the value of ω was gradually increased at the different levels of the multi-resolution pyramid, i.e., from the coarse to fine scales, in order to account for the fact that the likelihood of folding of the displacement field increases at the finest (final) level of the image pyramid with a larger number of control points.

To choose an optimum value of the above parameters, $\Delta \mathrm{d}\%$ was computed for different test values of that parameter while the other parameters were kept fixed. The test value that yielded the lowest error for the majority of the six images was used as the optimal setting for the RF-based NRIR and systematically applied to all data sets used for testing the accuracy of the method (cf. section III-B above).

D. Statistical analysis

To account for the non-Gaussian distribution of the tracking errors, non-parametric Friedman two-way analysis of variance (ANOVA) was used to assess whether the following differences in tracking errors were statistically significant:

a) Differences in errors while modifying grid aspect ratios/bending energy of the NRIR, where the two cofactors were i) solutions with different test values of grid aspect ratios/bending energy and ii) different bulk displacement magnitudes.

b) Differences in errors between RF-based NRIR and B-mode NRIR, where the cofactors were i) solutions prior to and after registration of the RF level and ii) different bulk displacement magnitudes.

c) Differences in displacement and strain errors between BM and NRIR where the two cofactors were i) motion estimation methods and ii) different motion/deformation magnitudes.

A value of $\mathrm{p} < 0.05$ was considered to be statistically significant and used as a threshold to run a post-hoc analysis by Tukey's honest significant difference (HSD) test in order to look for significant differences on changing the first cofactor for each of the above cases.

E. Implementation details

The multi-resolution pyramid was constructed with 9 levels. The transformation level complexity was implemented by changing the number of B-spline control grid points $\boldsymbol{\mu}_{\mathrm{ij}}$ (axial × lateral) from 11 × 4 at the coarsest level to 133 × 22 at the finest level. The corresponding inter-grid spacing $\sigma_{\mathrm{x}} \times \sigma_{\mathrm{y}}$ (axial samples × lateral lines) ranged from 1000 × 250 (coarsest)

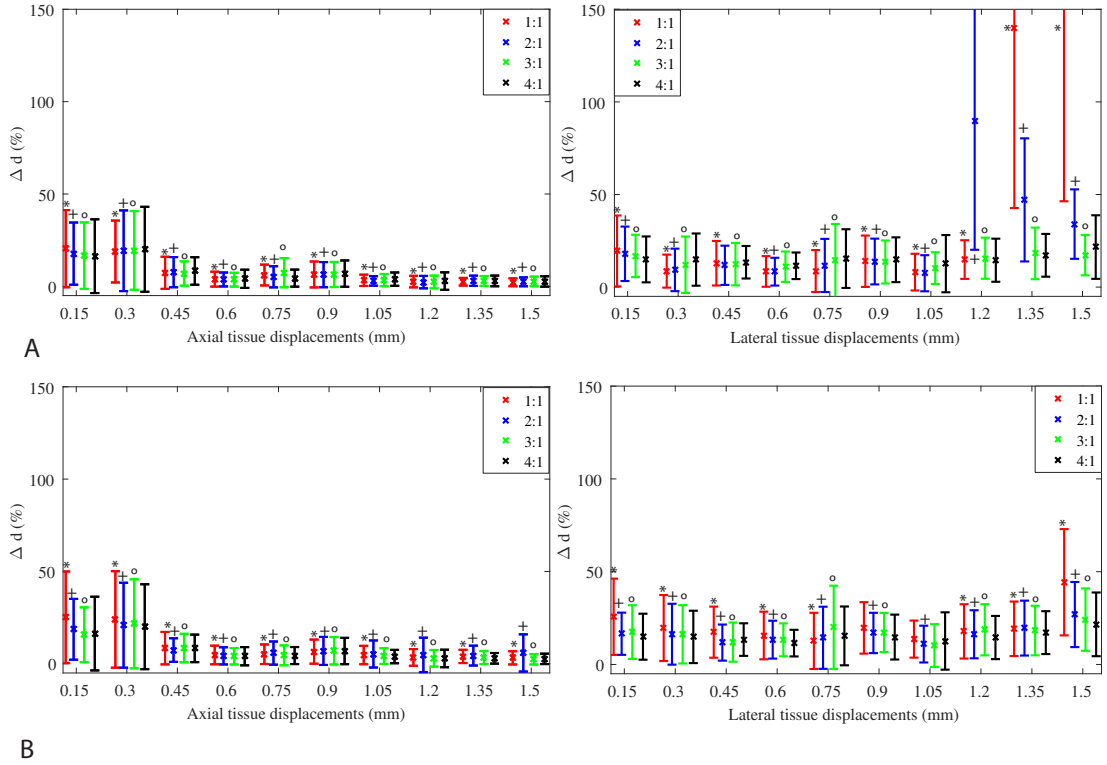

Fig. 3. Comparison of displacement errors Δd (%) on changing the aspect ratio (σ_x : σ_y) from 1:1 to 4:1 (final) for axial (left) and lateral (right) bulk displacements. Case A: increasing σ_x to reach an aspect ratio of 4:1. Case B: reducing σ_y to reach an aspect ratio of 4:1. *, + and o denote p<0.05, indicating significant difference of computed Δd (%) between each of the cases and 4:1 respectively.

to 60 $\times$ 10 (finest). To reduce the image level complexity, a 2D Gaussian kernel with a standard deviation of 30 samples $\times$ 4 lines was used at the coarsest level while no smoothing was used at the final level. The maximum size of the kernel at the coarsest level was chosen on the basis of the maximum motion present in the bulk motion modes. On the first 8 levels of the multi-resolution pyramid, envelope images were pre-aligned while the underlying RF samples were aligned on the finest level. The SSD and the BE energy were computed only inside the mask where the tissue was present.

F. Advantage of RF-based NRIR over B-mode NRIR

In order to demonstrate that also in an NRIR framework, RF data adds value to the accuracy of the motion estimates, the tracking error was determined at the final two scales of the multi-resolution approach: just prior to and after registration at the RF level, i.e., at the finest level of the envelope registration and the subsequent final (topmost) RF level.

G. Comparison of RF-based NRIR with block matching

In order to test the performance of the proposed RF-based NRIR against the state of the art, the same data sets were processed with a well-documented RF-based block matching (BM) approach as described in [24].

In brief, in this methodology, the 2D displacement field is computed between the fixed image, I_F and the moving image, I_M in two consecutive stages using the normalized cross-correlation (NCC) as a similarity metric [40] with subsequent cosine interpolation in both axial and lateral directions [41] in order to obtain sub-sample motion estimates. In the first stage, the axial displacement is estimated only using a 1D correlation kernel (295 samples; 20 samples window overlap). To reduce the decorrelation noise, a recorrelation method is used [23]. Subsequently, in a second stage, a 2D correlation kernel (295 axial samples $\times$ 15 lines; 20 samples window overlap) is used to estimate the residual axial and lateral displacements. The final displacements are then obtained as the sum of the displacement estimates from both stages. On both stages, a 2D search region of size $\pm$(103 samples $\times$ 12 lines) is used. Finally, both displacement components are filtered using a 2D median filter (10 displacement samples $\times$ 7 lines) and interpolated linearly to obtain the dimension of the RF data. The reader is kindly referred to [41] for a more detailed description of this BM methodology.

The same set of 6 synthetic images (as used in NRIR) were used to tune the parameters of the BM algorithm and these parameter settings were subsequently fixed in order to process the rest of the synthetic images.

Finally, time required for inter-frame motion tracking was recorded for both approaches. The main framework for both algorithms was written in C++. Although the RF-based NRIR computations were done on an Intel (R) Xeon E5, 2.5 GHz, 32 GB (RAM), 8 core machine, the BM computations were done on an Intel i7 (4770), 3.40 GHz, 4 core machine with 16 GB (RAM).

H. In-vivo application

The *in-vivo* feasibility of the proposed RF-based NRIR was tested using a dataset collected from a healthy volunteer using

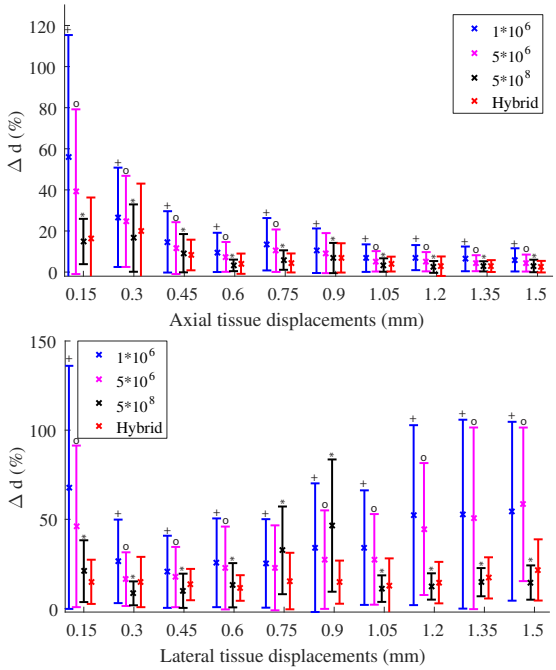

Fig. 4. Comparison of Δd% when using a constant BE weight ($\omega = 1\times10^6$, 5×10^6 and 5×10^8) or a variable BE weight (hybrid, see text for details) for (a) axial and (b) lateral bulk displacements. +, o and * denote p<0.05, indicating significant variation of Δd% between each of the settings and the hybrid setting respectively.

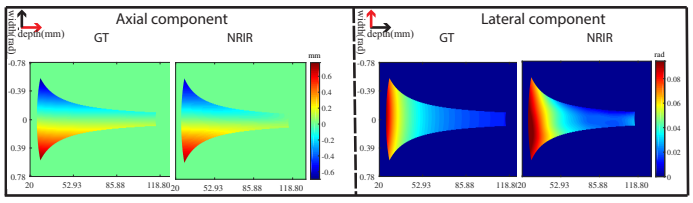

Fig. 5. An example of ground truth (GT) and estimated (NRIR), axial and lateral transformation fields in polar space for a lateral bulk displacement of d = 1.5 mm.

a 4 multi-transmit sequence implemented on the ULA-OP system [42], [43] in order to achieve a frame rate of 52 Hz over a 90 degree sector angle. The system was equipped with a 2 MHz phased array probe and the heart was scanned in a standard apical 4-chamber view. The RF data was sampled at 50 MHz resulting in RF frames of 8,994 samples $\times$ 176 lines. After RF-based NRIR, a region of interest (ROI) with a size of 10 mm $\times$ 10 mm was manually defined in the interventricular septum on the reconstructed B-mode images in order to extract both axial and lateral velocity profiles over the cardiac cycle as the average velocity value with this ROI. The resulting traces were temporally smoothed by a median filter with a length of 3 frames.

IV. Results

A. RF-based NRIR parameter optimization

The tracking errors for bulk axial and lateral inter-frame displacements estimated during the parameter optimization process on the anisotropy of the B-spline registration grid and the weighting of the regularization term are shown in Fig. 3

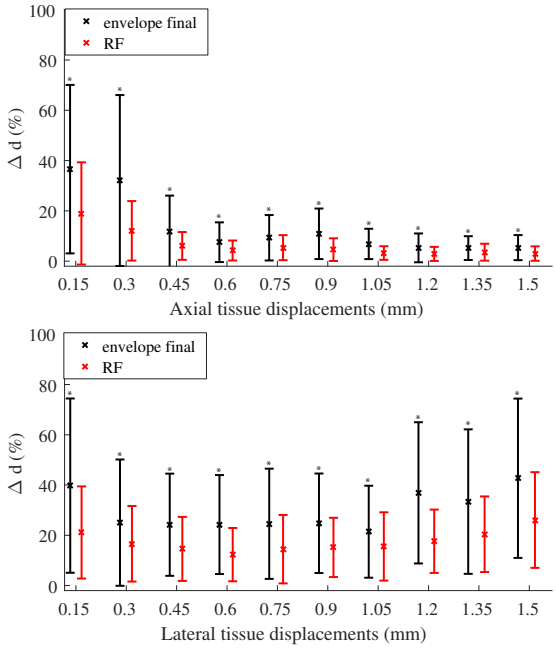

Fig. 6. Impact on Δd percentage on RF tracking post envelope tracking within the multi-resolution pyramid for both (a) axial and (b) lateral bulk displacements. * indicates p< 0.05.

and 4 respectively. An anisotropic aspect ratio of the B-spline grid was shown to reduce the registration error particularly for the estimates of the lateral component (Fig. 3, right column). Indeed for changing the grid aspect ratio from 1:1 to 4:1 (regardless of case A and B) for all axial displacements the mean error reduced by 1.6$\pm$1.2% and 0.1$\pm$0.77%; even more for the lateral displacements by 5.49$\pm$3.5% and 23.76$\pm$17.2%. Therefore, an anisotropic control grid with an aspect ratio of 4:1 was chosen as an optimal setting. For both bulk motion modes, a Friedman ANOVA analysis on Δd% obtained with different grid aspect ratios (case A and case B) and for all the motion magnitudes showed significant differences (p< 0.05). Again for both bulk motion modes, a post-hoc Tukey's HSD test showed errors obtained with an aspect ratio of 4:1 were significantly different (p< 0.05) (for case A and case B) than the rest of the grid aspect ratios.

For any value of the constant BE weight, the accuracy consistently increased with an increase in axial displacements (Fig. 4). In contrast, as ω reached 5×10^8, the error for the lateral inter-frame bulk displacements of 0.75 and 0.9 mm went up to 32% and 46% respectively. Overall, an ω with a value of 1×10^6, 5×10^6 and 5×10^8 for pyramid levels 1-3, 4-6 and 7-9 respectively seemed optimal. For both bulk motion modes, Friedman ANOVA analysis showed significant variation (p< 0.05) among Δd% estimated with different BE weights and over all motion magnitudes. A post-hoc Tukey's HSD test showed errors obtained with the hybrid setting of ω were significantly different than the rest of the three settings of ω.

B. Accuracy of RF-based NRIR

To visually assess the performance of the RF-based NRIR, an example of the axial and lateral transformation fields in

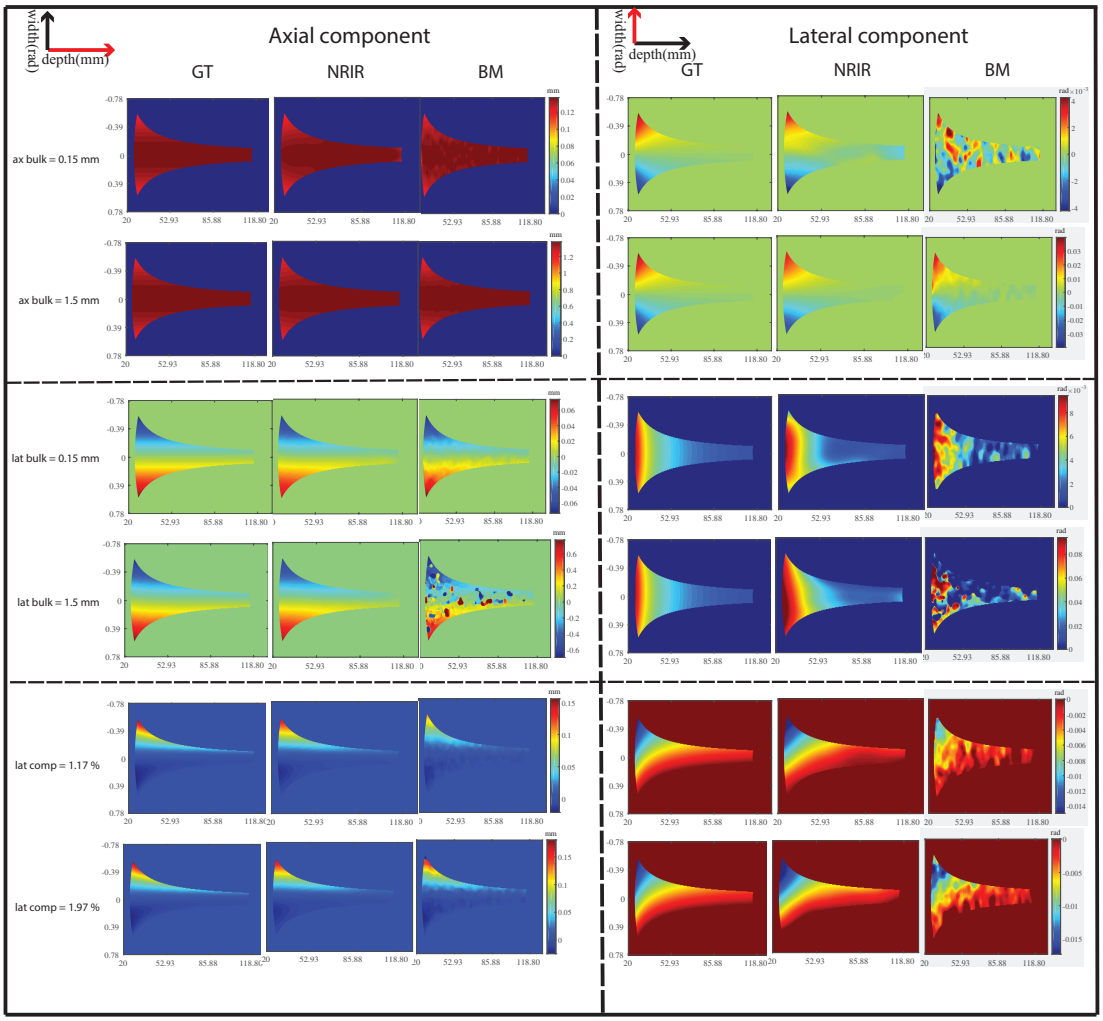

Fig. 7. Example of transformation fields in polar space for the minimum and maximum of the simulated inter-frame values for a) axial bulk motion, b) lateral bulk motion, and c) lateral compression. GT = ground truth, NRIR = non-rigid image registration, BM = block matching.

polar space for a lateral inter-frame bulk displacement of 1.5 mm is shown in Fig. 5.

In case of axial and lateral bulk displacements, the estimated displacement errors with respect to the ground truth were 7.25±8.01% and 15.06 ±12.62% respectively. In case of lateral deformation, the strain errors were 21.3±21.2%.

C. Advantage of RF-based NRIR over NRIR

Fig. 6 shows the increase in tracking accuracy of the NRIR methodology when moving from the finest scale of envelope registration to the RF registration. Overall, the final RF refinement in the motion estimate reduced the error by about 5.8±4.9% and 14.6±12.2% for the axial and lateral bulk motions respectively ($p < 0.05$). Again a post-hoc, Tukey's HSD test showed that the errors obtained from RF-based NRIR were significantly lower ($p<0.05$) than the ones estimated with NRIR registration.

D. Comparison of RF-NRIR with BM

To qualitatively compare the estimated motions obtained by both methods, examples of the displacement fields obtained in polar space for a single speckle realization are shown in Fig. 7. The top (a), middle (b) and the bottom (c) blocks represent three motion modes and each row represents the lowest and the highest simulated values from each mode. Each row contains the axial (first three columns) and lateral transformation fields (last three columns) for the ground truth and the two motion estimation methods. For axial displacements, the axial component of both the tracking algorithms were very competitive but the lateral component estimated by BM was noisy (top row, left column of Fig. 7). On the other hand, for lateral motion and lateral deformation modes, RF-based NRIR resulted in less noisy displacement fields for both axial and lateral components(right, middle and bottom rows respectively).

More quantitatively, these findings are summarized in Fig. 8. For all axial and lateral motion amplitudes, RF-based NRIR showed smaller estimation errors than BM. For both approaches, the estimation error decreased for increasing inter-frame displacement in the axial direction while there was an optimal inter-frame displacement range for estimates of the lateral component. The estimation error for BM was higher than NRIR by 24.9% and 68.8% for the motion mode at the

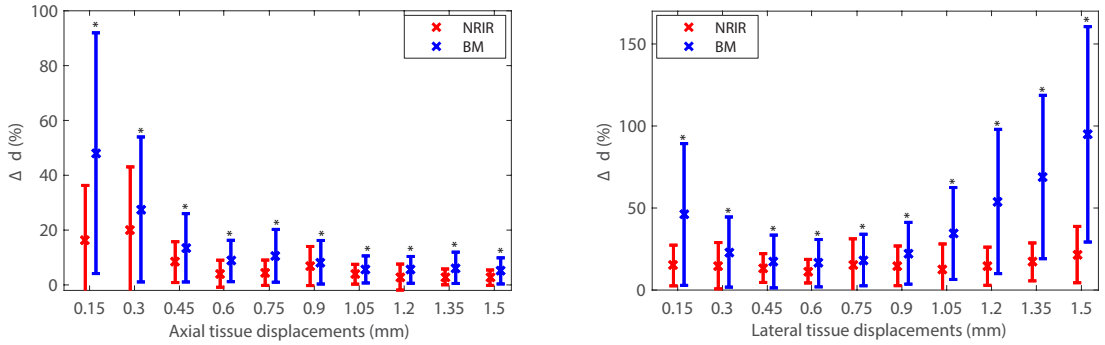

Fig. 8. Displacement errors, Δd (%) for all the simulated a) axial and b) lateral bulk displacements in NRIR and BM. * indicates p$<$ 0.05.

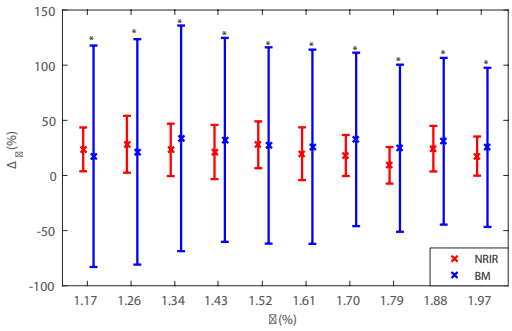

Fig. 9. Mean and standard deviation of the relative strain errors for the simulated range ε for both NRIR and BM. * indicates p$<$ 0.05.

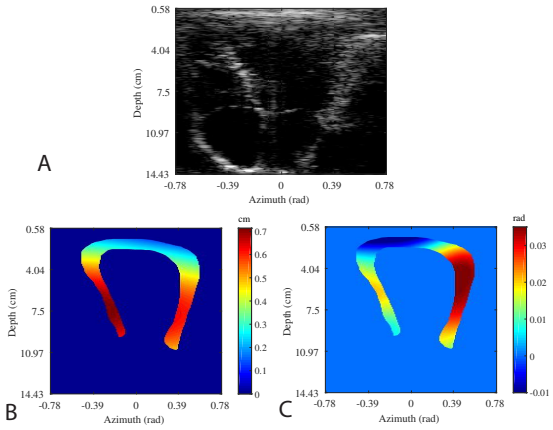

Fig. 10. Top: (A) Non-scan converted image at end-systole. Bottom: (B) axial and (C) lateral cumulative displacement fields at end-systolic (ES), shown only at the myocardium.

extremities of the tested lateral motion range. It can be seen that for the estimated lateral motion the optimum range was more pronounced for the BM approach.

Fig. 9 shows a comparison of the mean and the standard deviation of the relative strain errors for both motion estimators. Although the average strain estimates were very competitive between both approaches, the variance of the estimation error obtained with BM was 66.37% higher than that of RF-based NRIR.

For all three motion modes, a Friedman ANOVA yielded statistically significant difference in estimation errors i.e.,p $<$ 0.05, between both the methods and for all displacement magnitudes. A post-hoc analysis with Tukey's HSD test showed the errors estimated by NRIR differed significantly (p$<$0.05) than BM for all three motion modes.

The average inter-frame registration time for RF-based NRIR and BM were 2.3 mins and 0.23 min respectively.

E. In-vivo application of RF-based NRIR

Fig. 10 shows a non-scan converted frame of the normal volunteer at end-systole (ES). The estimated axial and the lateral cumulative displacement fields at ES, corresponding to the myocardium are shown below. Subsequently, Fig. 11 shows a B-mode frame at end-diastole, with the ROI (red) in which the tracking was evaluated. The extracted axial and lateral velocity traces are also shown. Both profiles showed a clear systolic (S′), early diastolic (E′) and late diastolic (A′) waves.

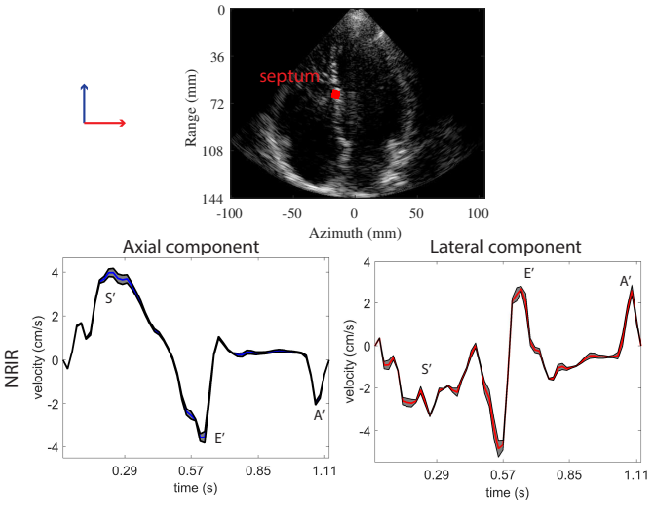

Fig. 11. Top: B-mode frame of a healthy volunteer with the ROI (red) at septum. Bottom: Mean axial (blue) and lateral (red) velocity traces computed at the ROI (10 mm $\times$ 10 mm) using the RF-based NRIR. The respective standard deviation of the velocity estimates within the ROI are denoted with the black lines.

V. Discussion and Conclusion

This study demonstrated the performance of an RF-based NRIR and contrasted it against a state of the art BM solution using synthetic data sets. The main advantage of the NRIR

approach showed to be a more robust estimate of the lateral motion and deformation modes while both approaches were very competitive to estimate motion in the axial direction. The gain in accuracy showed to be most pronounced for relatively large inter-frame lateral displacements (cf. Fig. 8) where BM had more difficulties in obtaining correct estimates likely due to the lack of intrinsic regularization during the estimation process in combination with peak hopping errors that are more likely to occur when large motions are involved. The findings are in line with our previous findings comparing NRIR with BM on B-mode images [16]. NRIR improved the lateral estimates significantly with respect to BM but still the lateral strain errors were higher than the clinically acceptable limits. As such, despite this improvement, the lateral estimates are not optimum yet to be used in a clinical context.

The main incentive of this study to process RF data was to increase tracking accuracy as reported by others using speckle tracking approaches (e.g., [17], [18], [44]). In this study, we could indeed demonstrate that RF-based NRIR increases accuracy with respect to NRIR on the envelope data alone for both motion components. Not surprisingly, the gain of RF-based NRIR was particularly pronounced for small axial inter-frame displacements (cf. Fig. 6).

Applying NRIR on RF data in contrast to scan-converted data implied motion estimation on images in beam space where the tissue motion is higher in the near field compared to the far field. Secondly, the difference in absolute intensities of the RF images affects the intensity based similarity measure used in our NRIR framework and therefore the convergence tolerance factor of the optimizer needs to be adapted accordingly.

Two challenges met when applying the NRIR framework on RF data were the computational burden of the method, particularly when applied to large images such RF frames, and the anisotropic nature of the registration problem. These problems were dealt with in the proposed RF-based NRIR solution by making use of an analytical version of the regularizer (as previously presented in [32]) and making use of an anisotropic registration grid with an aspect ratio of 4:1 respectively. A final modification required to be made to the NRIR framework was that the weighting parameter determining the balance between image and prior information was made variable depending on the level in the coarse-to-fine processing. Although to our knowledge, such a dynamic weighting has not been described before, it has been shown to be important in order to get accurate RF-based NRIR estimates. The underlying reason for this is likely that to capture larger displacements, a lower ω on coarser levels imposed less boundary conditions and indeed a higher omega in these levels imposed additional constraints leading to optimization failure. However, at the finer grid resolution the chance of the folding of the transformation field increased and a lower ω increased the error. As such, the combination of a low and high ω at the coarsest and the finest scales respectively led to an optimal solution.

Finally, to prove that the developed RF-based NRIR motion estimator can also be used on real RF data set recorded *in-vivo*, an initial feasibility test was performed. This test showed that both axial and lateral velocity traces of the septal wall could be extracted and both showed a normal physiologic pattern. An extensive evaluation of the proposed motion estimator *in-vivo* is the topic of ongoing work.

One of the limitations of the study was that the *in-silico* images were simulated under ideal consideration, i.e., noise and non-linearity were not considered. Nevertheless, the *in-vivo* feasibilty showed clinically promising results. Additionally, despite the fact that the RF-based NRIR made use of an analytic expression of the computation of the bending energy in order to increase the speed, it remains significantly slower than BM. Although the computational load cannot be compared directly as both algorithms were run on distinct computers (i.e., in the respective labs involved in this study), it seems clear that the proposed NRIR motion estimator is slower than BM as it solves the motion estimation problem iteratively rather than in a single iteration. Nevertheless, if calculation time was considered a practical bottleneck then the computations can still be extended to GPU.

In conclusion, an RF-based NRIR motion estimator was proposed and shown to outperform BM in terms of accuracy for lateral motion and deformation estimates in synthetic data sets. Moreover, this estimator was proven to outperform its B-mode correlate. An initial application of the proposed estimator in clinical data, demonstrated its feasibility *in-vivo*.

VI. Acknowledgement

This work was supported by funding from the European Research Council, under the European Seventh Framework Programme (HeartMAPAS; FP7/2007-2013/ERC Grant Agreement number 281748) awarded to the KU Leuven. We like to thank Prof. Tortoli, for providing the *in-vivo* dataset.

References

[1] George R Sutherland, Giovanni Di Salvo, Piet Claus, Jan D'hooge, and Bart Bijnens. Strain and strain rate imaging: a new clinical approach to quantifying regional myocardial function. *Journal of the American Society of Echocardiography*, 17(7):788–802, 2004.

[2] Goo-Yeong Cho, Thomas H Marwick, Hyun-Sook Kim, Min-Kyu Kim, Kyung-Soon Hong, and Dong-Jin Oh. Global 2-dimensional strain as a new prognosticator in patients with heart failure. *Journal of the American College of Cardiology*, 54(7):618–624, 2009.

[3] Jonathan Chan, Lizelle Hanekom, Chiew Wong, Rodel Leano, Goo-Yeong Cho, and Thomas H Marwick. Differentiation of subendocardial and transmural infarction using two-dimensional strain rate imaging to assess short-axis and long-axis myocardial function. *Journal of the American College of Cardiology*, 48(10):2026–2033, 2006.

[4] Matthew S Suffoletto, Kaoru Dohi, Maxime Cannesson, Samir Saba, and John Gorcsan. Novel speckle-tracking radial strain from routine black-and-white echocardiographic images to quantify dyssynchrony and predict response to cardiac resynchronization therapy. *Circulation*, 113(7):960–968, 2006.

[5] Javier Ganame, Piet Claus, Benedicte Eyskens, Anne Uyttebroeck, Marleen Renard, Jan Dhooge, Marc Gewillig, Bart Bijnens, George R Sutherland, and Luc Mertens. Acute cardiac functional and morphological changes after anthracycline infusions in children. *The American journal of cardiology*, 99(7):974–977, 2007.

[6] Laurence N Bohs and Gregg E Trahey. A novel method for angle independent ultrasonic imaging of blood flow and tissue motion. *IEEE Transactions on Biomedical Engineering*, 38(3):280–286, 1991.

[7] Berthold KP Horn and Brian G Schunck. Determining optical flow. *Artificial intelligence*, 17(1-3):185–203, 1981.

[8] Jean Meunier, Michel Bertrand, Guy Mailloux, and Robert Petitclerc. Assessing local myocardial deformation from speckle tracking in echography. In *Medical Imaging II*, pages 20–31. International Society for Optics and Photonics, 1988.

[9] Martino Alessandrini, Hervé Liebgott, Daniel Barbosa, and Olivier Bernard. Monogenic phase based optical flow computation for myocardial motion analysis in 3D echocardiography. In *International Workshop on Statistical Atlases and Computational Models of the Heart*, pages 159–168. Springer, 2012.

[10] Chihiro Kasai, Koroku Namekawa, Akira Koyano, and Ryozo Omoto. Real-time two-dimensional blood flow imaging using an autocorrelation technique. *IEEE Transactions on sonics and ultrasonics*, 32(3):458–464, 1985.

[11] Manish Bansal, Leanne Jeffriess, Rodel Leano, Julie Mundy, and Thomas H Marwick. Assessment of myocardial viability at dobutamine echocardiography by deformation analysis using tissue velocity and speckle-tracking. *JACC: Cardiovascular Imaging*, 3(2):121–131, 2010.

[12] Jonathan Chan, Lizelle Hanekom, Chiew Wong, Rodel Leano, Goo-Yeong Cho, and Thomas H Marwick. Differentiation of subendocardial and transmural infarction using two-dimensional strain rate imaging to assess short-axis and long-axis myocardial function. *Journal of the American College of Cardiology*, 48(10):2026–2033, 2006.

[13] Thomas H Marwick, Rodel L Leano, Joseph Brown, Jing-Ping Sun, Rainer Hoffmann, Peter Lysyansky, Michael Becker, and James D Thomas. Myocardial strain measurement with 2-dimensional speckle-tracking echocardiography: definition of normal range. *JACC: Cardiovascular Imaging*, 2(1):80–84, 2009.

[14] Martino Alessandrini, Adrian Basarab, Hervé Liebgott, and Olivier Bernard. Myocardial motion estimation from medical images using the monogenic signal. *IEEE Transactions on Image Processing*, 22(3):1084–1095, 2013.

[15] Brecht Heyde, Piet Claus, Ruta Jasaityte, Daniel Barbosa, Stefaan Bouchez, Michael Vandenheuvel, Patrick Wouters, Frederik Maes, and Jan D'hooge. Motion and deformation estimation of cardiac ultrasound sequences using an anatomical B-spline transformation model. In *2012 9th IEEE International Symposium on Biomedical Imaging (ISBI)*, pages 266–269. IEEE, 2012.

[16] Brecht Heyde, Ruta Jasaityte, Daniel Barbosa, Valérie Robesyn, Stefaan Bouchez, Patrick Wouters, Frederik Maes, Piet Claus, and Jan D'hooge. Elastic image registration versus speckle tracking for 2-D myocardial motion estimation: A direct comparison in vivo. *IEEE Trans. Med. Imaging*, 32(2):449–459, 2013.

[17] Bhaskar S Ramamurthy and Gregg E Trahey. Potential and limitations of angle-independent flow detection algorithms using radio-frequency and detected echo signals. *Ultrasonic Imaging*, 13(3):252–268, 1991.

[18] Weichuan Yu, Ping Yan, Albert J Sinusas, Karl Thiele, and James S Duncan. Towards pointwise motion tracking in echocardiographic image sequences–comparing the reliability of different features for speckle tracking. *Medical image analysis*, 10(4):495–508, 2006.

[19] Chi Ma and Tomy Varghese. Comparison of cardiac displacement and strain imaging using ultrasound radiofrequency and envelope signals. *Ultrasonics*, 53(3):782–792, 2013.

[20] Stian Langeland, Jan D'hooge, Tom Claessens, Piet Claus, Pascal Verdonck, Paul Suetens, George R Sutherland, and Bart Bijnens. RF-based two-dimensional cardiac strain estimation: a validation study in a tissue-mimicking phantom. *IEEE transactions on ultrasonics, ferroelectrics, and frequency control*, 51(11):1537–1546, 2004.

[21] Josef Korinek, Jianwen Wang, Partho P Sengupta, Chinami Miyazaki, Jesper Kjaergaard, Eileen McMahon, Theodore P Abraham, and Marek Belohlavek. Two-dimensional strain–a doppler-independent ultrasound method for quantitation of regional deformation: validation in vitro and in vivo. *Journal of the American Society of Echocardiography*, 18(12):1247–1253, 2005.

[22] Richard GP Lopata, Maartje M Nillesen, Hendrik HG Hansen, Inge H Gerrits, Johan M Thijssen, and Chris L de Korte. Performance of two dimensional displacement and strain estimation techniques using a phased array transducer. *Ultrasound in medicine & biology*, 35(12):2031–2041, 2009.

[23] Jianwen Luo, Wei-Ning Lee, and Elisa E Konofagou. Fundamental performance assessment of 2-D myocardial elastography in a phased-array configuration. *IEEE transactions on ultrasonics, ferroelectrics, and frequency control*, 56(10):2320–2327, 2009.

[24] Jianwen Luo and Elisa E Konofagou. A fast normalized cross-correlation calculation method for motion estimation. *IEEE transactions on ultrasonics, ferroelectrics, and frequency control*, 57(6):1347–1357, 2010.

[25] Hideyuki Hasegawa. Phase-sensitive 2D motion estimators using frequency spectra of ultrasonic echoes. *Applied Sciences*, 6(7):195, 2016.

[26] Michael S Richards and Marvin M Doyley. Non-rigid image registration based strain estimator for intravascular ultrasound elastography. *Ultrasound in medicine & biology*, 39(3):515–533, 2013.

[27] Brecht Heyde, Martino Alessandrini, Ling Tong, and Jan D'hooge. RF-based motion estimation using non-rigid image registration techniques: In-silico and in-vivo feasibility. In *Ultrasonics Symposium (IUS), 2014 IEEE International*, pages 2280–2283. IEEE, 2014.

[28] Bidisha Chakraborty, Zhi Liu, Brecht Heyde, Jianwen Luo, and Jan D'hooge. 2D RF-based non-rigid image registration for cardiac motion estimation: Comparison against block matching. In *Ultrasonics Symposium (IUS), 2016 IEEE International*, pages 1–4. IEEE, 2016.

[29] Daniel Rueckert, Luke I Sonoda, Carmel Hayes, Derek LG Hill, Martin O Leach, and David J Hawkes. Nonrigid registration using free-form deformations: application to breast MR images. *IEEE Trans. Med. Imaging*, 18(8):712–721, 1999.

[30] Hava Lester and Simon R Arridge. A survey of hierarchical non-linear medical image registration. *Pattern recognition*, 32(1):129–149, 1999.

[31] Richard H Byrd, Peihuang Lu, Jorge Nocedal, and Ciyou Zhu. A limited memory algorithm for bound constrained optimization. *SIAM Journal on Scientific Computing*, 16(5):1190–1208, 1995.

[32] Bidisha Chakraborty, Brecht Heyde, Martino Alessandrini, and Jan D'hooge. Fast myocardial strain estimation from 3D ultrasound through elastic image registration with analytic regularization. In *SPIE Medical Imaging*, pages 979006–979006. International Society for Optics and Photonics, 2016.

[33] James A Shackleford, Qi Yang, Ana M Lourenço, Nadya Shusharina, Nagarajan Kandasamy, and Gregory C Sharp. Analytic regularization of uniform cubic B-spline deformation fields. In *MICCAI 2012*, volume 7511, pages 122–129. Springer, 2012.

[34] Bernard J Oosterveld, Jos M Thijssen, and Wim A Verhoef. Texture of B-mode echograms: 3-D simulations and experiments of the effects of diffraction and scatterer density. *Ultrasonic Imaging*, 7(2):142–160, 1985.

[35] Hang Gao, Hon Fai Choi, Piet Claus, Steven Boonen, Siegfried Jaecques, G Harry Van Lenthe, Georges Van der Perre, Walter Lauriks, and Jan D'hooge. A fast convolution-based methodology to simulate 2-D/3-D cardiac ultrasound images. *IEEE transactions on ultrasonics, ferroelectrics, and frequency control*, 56(2):404–409, 2009.

[36] Luis Caballero, Seisyou Kou, Raluca Dulgheru, Natalia Gonjilashvili, George D Athanassopoulos, Daniele Barone, Monica Baroni, Nuno Cardim, Jose Juan Gomez de Diego, Maria Jose Oliva, et al. Echocardiographic reference ranges for normal cardiac doppler data: results from the NORRE study. *Eur Heart J Cardiovasc Imaging*, page jev083, 2015.

[37] GS Sawhney. *Fundamental of biomedical engineering*. New Age International, 2007.

[38] Teerapat Yingchoncharoen, Shikhar Agarwal, Zoran B Popović, and Thomas H Marwick. Normal ranges of left ventricular strain: a meta-analysis. *Journal of the American Society of Echocardiography*, 26(2):185–191, 2013.

[39] Brecht Heyde, Stefaan Bouchez, Sabine Thieren, Michael Vandenheuvel, Ruta Jasaityte, Daniel Barbosa, Piet Claus, Frederik Maes, Patrick Wouters, and Jan D'hooge. Elastic image registration to quantify 3-D regional myocardial deformation from volumetric ultrasound: experimental validation in an animal model. *Ultrasound in Med. & Biol.*, 39(9):1688–1697, 2013.

[40] Francesco Viola and William F Walker. A comparison of the performance of time-delay estimators in medical ultrasound. *IEEE transactions on ultrasonics, ferroelectrics, and frequency control*, 50(4):392–401, 2003.

[41] Zhi Liu, Chengwu Huang, and Jianwen Luo. A systematic investigation of lateral estimation using various interpolation approaches in conventional ultrasound imaging. *IEEE Transactions on Ultrasonics, Ferroelectrics, and Frequency Control*, 2017.

[42] Ling Tong, Alessandro Ramalli, Piero Tortoli, Guiseppe Fradella, Sabina Caciolli, Jianwen Luo, and Jan D'hooge. Wide-angle tissue doppler imaging at high frame rate using multi-line transmit beamforming: An experimental validation in vivo. *IEEE transactions on medical imaging*, 35(2):521–528, 2016.

[43] Piero Tortoli, Luca Bassi, Enrico Boni, Alessandro Dallai, Francesco Guidi, and Stefano Ricci. ULA-OP: An advanced open platform for ultrasound research. *IEEE transactions on ultrasonics, ferroelectrics, and frequency control*, 56(10):2207–2216, 2009.

[44] Tomy Varghese and Jonathan Ophir. Characterization of elastographic noise using the envelope of echo signals. *Ultrasound in medicine & biology*, 24(4):543–555, 1998.

[45] An Elena, Dirk Loeckxa, Hon Fai Choib, Hang Gaob, Piet Clausb, Frederik Maesa, Paul Suetensa, and Jan Dhoogeb. Estimation of 3d cardiac deformation using spatio-temporal elastic registration of non-scanconverted ultrasound data. In *Proc. of SPIE Vol*, volume 6920, pages 69200R–1, 2008.